Geosciences Journal
Vol. 11, No. 3, p. 185 − 199, September 2007

Origin of E-MORB in a fossil spreading center: the Antarctic-Phoenix Ridge, Drake Passage, Antarctica

Won Hie Choe, Jong Ik Lee* — *Korea Polar Research Institute, KORDI, Songdo Techno Park 7-50, Songdo-dong, Yeonsu-gu, Incheon 406-840, Korea*
Mi Jung Lee — *Korea Institute of Geoscience and Mineral Resources (KIGAM), Gajeong-dong 30, Yuseong-gu, Daejeon 305-350, Korea*
Soon Do Hur, Young Keun Jin — *Korea Polar Research Institute, KORDI, Songdo Techno Park 7-50, Songdo-dong, Yeonsu-gu, Incheon 406-840, Korea*

ABSTRACT: The fossilized Antarctic-Phoenix Ridge (APR) with three segments (P1, P2, and P3), Drake Passage, is distant from the known hotspots, and consists of older N-MORB formed prior to the extinction of spreading and younger E-MORB after extinction. The older N-MORB (3.5-6.4 Ma) occur in the southeastern flank of the P3 segment (PR3) and the younger E-MORB (1.4-3.1 Ma) comprise a huge seamount at the former ridge axis of the P3 segment (SPR) and a big volcanic edifice at the northwestern flank of the P2 segment (PR2). The PR3 basalts have higher Mg#, K/Ba, and CaO/Al_2O_3 and lower Zr/Y, Sr, and $Na_{8.0}$ (fractionation-corrected Na_2O to 8.0% MgO) with slight enrichment in incompatible elements and almost flat REE patterns. The SPR and PR2 basalts are highly enriched in incompatible elements and LREE. The extinction of spreading at 3.3 Ma seems to have led to a temporary magma oversupply with E-MORB signatures. Geochemical signatures such as Ba/TiO_2, Ba/La, and Sm/La suggest the heterogeneity of upper mantle and formation of E-MORB by higher contribution of enriched materials (e.g., metasomatized veins) to mantle melting than the N-MORB environment. E-MORB magmas beneath the APR seem to have been produced by low-degree melting at deeper regime, where enriched materials have preferentially participated in the melting. The occurrence of E-MORB at the APR is a good example to better understand what kinds of magmatism would occur in association with extinction of the ridge spreading.

Key words: Antarctic-Phoenix Ridge, extinction of spreading, E-MORB, low-degree melting, mantle heterogeneity

1. INTRODUCTION

Compared to other mantle products derived from subduction zones or intra-plates, mid-ocean ridge basalts (MORB), which represent the end product of decompression melting of upwelling upper mantle, show relatively small geochemical variations. MORB generally have low abundance of incompatible elements, low radiogenic Sr, and high radiogenic Nd, suggesting that the oceanic upper mantle is relatively depleted (Zindler and Hart, 1986). However, common occurrences of incompatible element enriched-type MORB (E-MORB) in all ridges worldwide indicate that this depleted MORB mantle (DMM) is compositionally heterogeneous (e.g., Donnelly et al., 2004; Kent, 2004, Janney, 2005). The origin of E-MORB has been generally explained by interaction of plumes derived from deep mantle with depleted upper mantle source of normal mid-ocean ridge basalts (N-MORB) (e.g., Rhodes et al., 1990; Douglass et al., 1999).

The origin of E-MORB which does not have any relations with known plumes is yet controversial. E-MORB, not associated with hotspots, are widespread, and occur on both fast- and slow-spreading ridges: e.g., fast-spreading East Pacific Rise (Niu et al., 1999) and slow-spreading Mid-Atlantic Ridge (Donnelly et al., 2004). Hanson and Langmuir (1978) first suggested that E-MORB reflect preferential melting of "enriched" veins in the mantle. Recently, most workers agree that mantle convection and crustal recycling are primary mechanisms that create the enriched heterogeneities as "blobs" or "veins" deep in the mantle (Niu et al., 1999 and references therein).

In the Drake Passage, between South America and Antarctica, there is a remnant of the once-extensive spreading center, the Antarctic-Phoenix Ridge (APR), consisting of both N-MORB and E-MORB (Fig. 1). The APR appears to have become extinct at some time during the Pliocene (Larter and Barker, 1991). As a result, a small remnant of the former Phoenix plate, confined between the Shackleton and Hero Fracture zones, has become welded into the Antarctic plate. On the basis of reconnaissance precision echo sounder records and magnetic data, Larter and Barker (1991) concluded that the three inactive segments of the APR are remnants, which Livermore et al. (2000) refer to as P1, P2, and P3 from northeast to southwest. However, recent geomorphological and magnetic data still argue whether the extinction of spreading at the three segments occurred simultaneously or not (Livermore et al., 2000 and references therein). Compared to many results from geophysical investigations, geochemical relations between N-MORB and E-MORB of the APR are poorly constrained.

Because of the presence of strong Antarctic Circumpolar Current preventing thick sediment accumulations in the Drake Passage, the fossil spreading centers of the APR are uniquely exposed to bathymetric mapping and dredging. During the 1999-2000 austral summer season, a half of the

*Corresponding author: jilee@kopri.re.kr

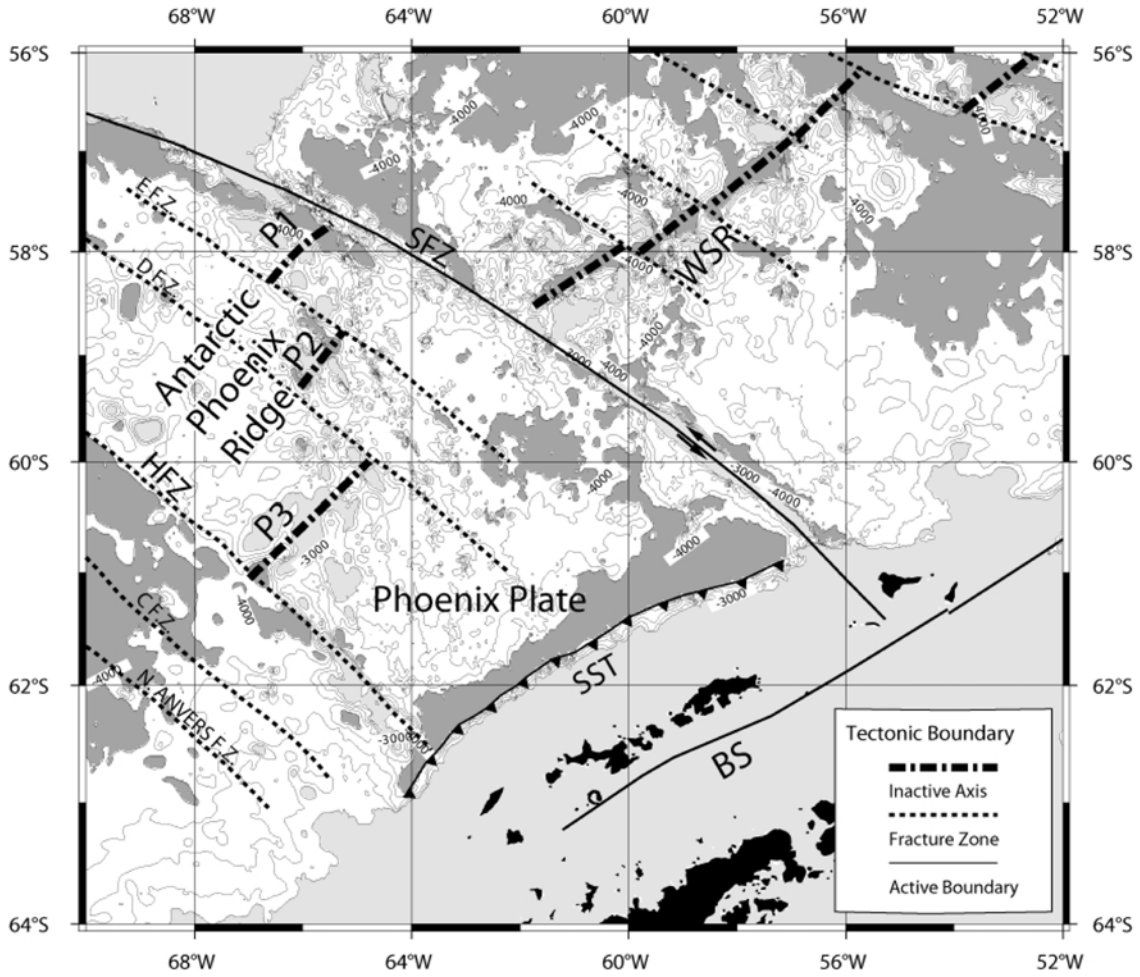

Fig. 1. Tectonic boundary map over the bathymetry using satellite altimetry in Drake Passage (modified from Smith and Sandwell, 1994). Dark gray color denotes the area below 4000 m depth and light gray above 3000 m. Solid, thin dotted and heavy dotted lines represent active boundaries, fracture zones and inactive spreading axis, respectively. P1, P2 and P3 denote three segments of the Antarctic-Phoenix Ridge. Abbreviations: SFZ, Shackleton Fracture Zone; HFZ, Hero Fracture Zone; SST, South Shetland Trench; WSR, West Scotia Ridge; BS, Bransfield Strait; DFZ, D Fracture Zone; EFZ, E Fracture Zone.

P3 segment was mapped using a multibeam echo sounder fitted to the Korean research vessel R/V *Onnuri* (Kim, 2005). During the 2000-2001 and 2002-2003 summer cruises with R/V *Yuzhmorgeologiya*, submarine fresh lavas from the P2 and P3 segments have been intensively dredged, and geochemically investigated.

In this paper, we report the geochemical characteristics of both N-type and E-type MORB in the APR, Drake Passage. The analyzed samples have been systematically collected in order to delineate temporal and spatial changes in the compositions of magmas generated from the APR, particularly with respect to the extinction of spreading. Our data will provide clues on the heterogeneity of upper mantle beneath the APR.

2. TECTONIC SETTING

The Phoenix plate was one of the major Pacific Ocean plates, created by seafloor spreading since the Jurassic. Previous works (Barker, 1982; Larter and Barker, 1991) suggested that the three remaining segments of the APR became inactive following collisions between more southerly ridge segments and an active subduction zone to the southwest of the Hero Fracture Zone (HFZ). Continuous subduction at the South Shetland Trench, together with oceanward retreat of the hinge of subduction, led to the rifting and separation of a sliver of the Antarctic Peninsula margin carrying the South Shetland Islands, and the opening of the Bransfield Strait marginal basin (Maldonado et al., 1994). Magnetic anomaly profiles crossing P1 and P3 suggested a ridge extinction at ca. 4.5 Ma (Barker, 1982) or 3.5 Ma (Larter and Barker, 1991), following a period of declining spreading rates. Livermore et al. (2000) insisted a synchronous extinction of all three segments at the time of magnetic chron C2A (3.3 Ma), using new bathymetry and magnetic anomaly data. This temporal constraint is synchronous with a ridge-trench collision at the south of the

HFZ. Kim (2005) suggested that the extinction of the P3 segment occurred at 3.6 Ma, based on the absence of C2A magnetic chron at the axis.

The three segments between HFZ and Shakleton Fracture Zone (SFZ) show typical slow-moving discontinuities of the sharp boundaries and depressions (Livermore et al., 2000). The APR evolved from an intermediate- to a slow-spreading ridge. It has the characteristics of both intermediate-spreading ridges far away from the ridge axis and slow-spreading ridges near the axis. At the terminal stage of spreading, the spreading rates were different between the southern and northern flanks, suggesting asymmetric spreading of the Phoenix Ridge. The most significant reductions in spreading rate occurred among anomalies C4-C3A, C3A-C3, and C3-C2A.

3. MORPHOLOGY AND K-AR AGE

The P2 segment begins at Fracture Zone D and runs over a distance of 40 km to northeast (Fig. 2). The rift valley along the axis has a depth of ca. 2500 m. The off-axis morphology of the P2 segment is generally comparable to that of fast- or intermediate-spreading ridges dominated by linear, axis-parallel magmatic ridges and straight, sharply defined fracture zones (Livermore et al., 2000). The near-axis morphology of the P2 segment shows very high relief, and is anomalous when compared to either fast- or slow-spreading ridges elsewhere. The axial region is flanked by two great ridges; that on the northwestern flank rises to an unexpectedly shallow 570 m depth near the segment center, and that on the southeastern flank is deeper than 1500 m. Livermore et al. (2000) pointed out that the high-relief paired ridges on the P2 segment resulted from abrupt reduction in spreading rates, when non-magmatic extension became dominant (Thatcher and Hill, 1995).

Basalt samples (PR2) at the P2 segment were systematically collected from the inner wall of the northwestern flank. The K-Ar whole-rock ages for these basalts range from 2.1 to 1.4 Ma, and are generally younger toward the ridge axis (Choe et al., 2005).

New bathymetry was obtained over the intersection between the P3 segment and the HFZ during 1999-2000 austral summer, using a SEABEAM 2000 multibeam sounder on the Korean R/V *Onnuri* (Kim, 2005). The P3 segment begins at

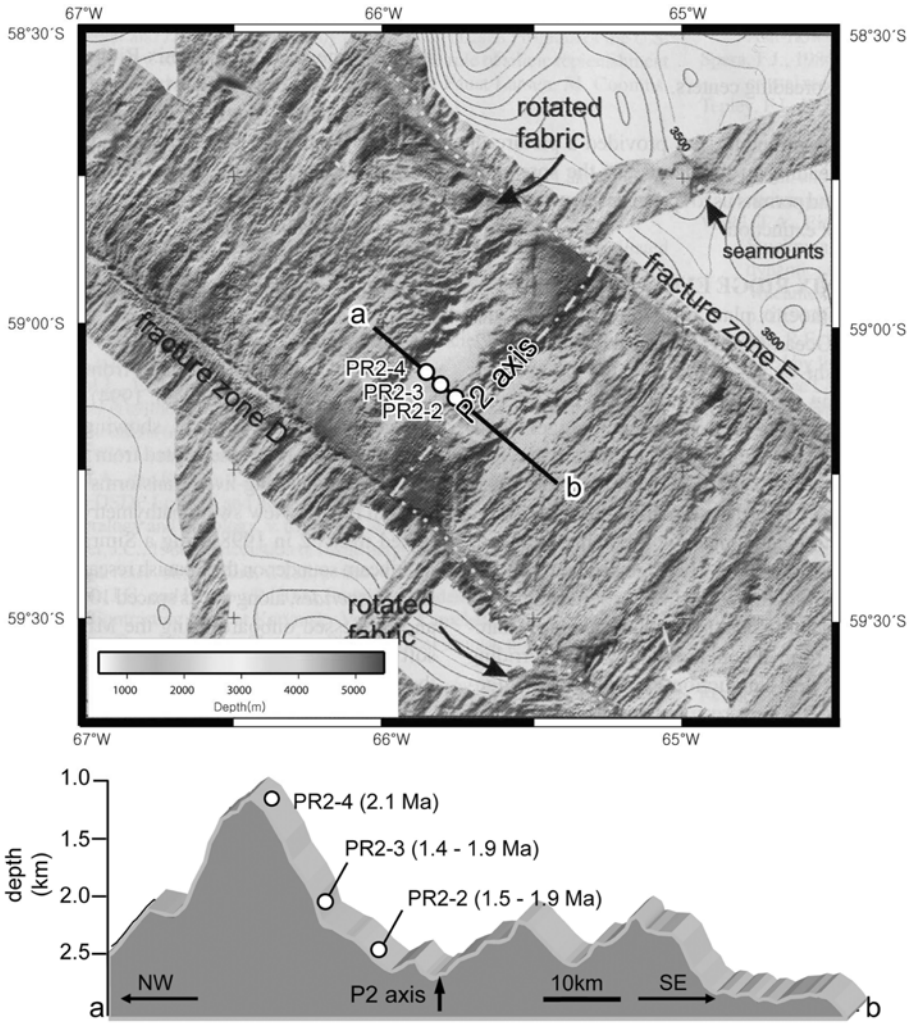

Fig. 2. Bathymetry and depth profile of the P2 segment, modified from Livermore et al. (2000). Circles represent sample locations and the K-Ar ages at these sites are shown in parentheses (Choe et al., 2005).

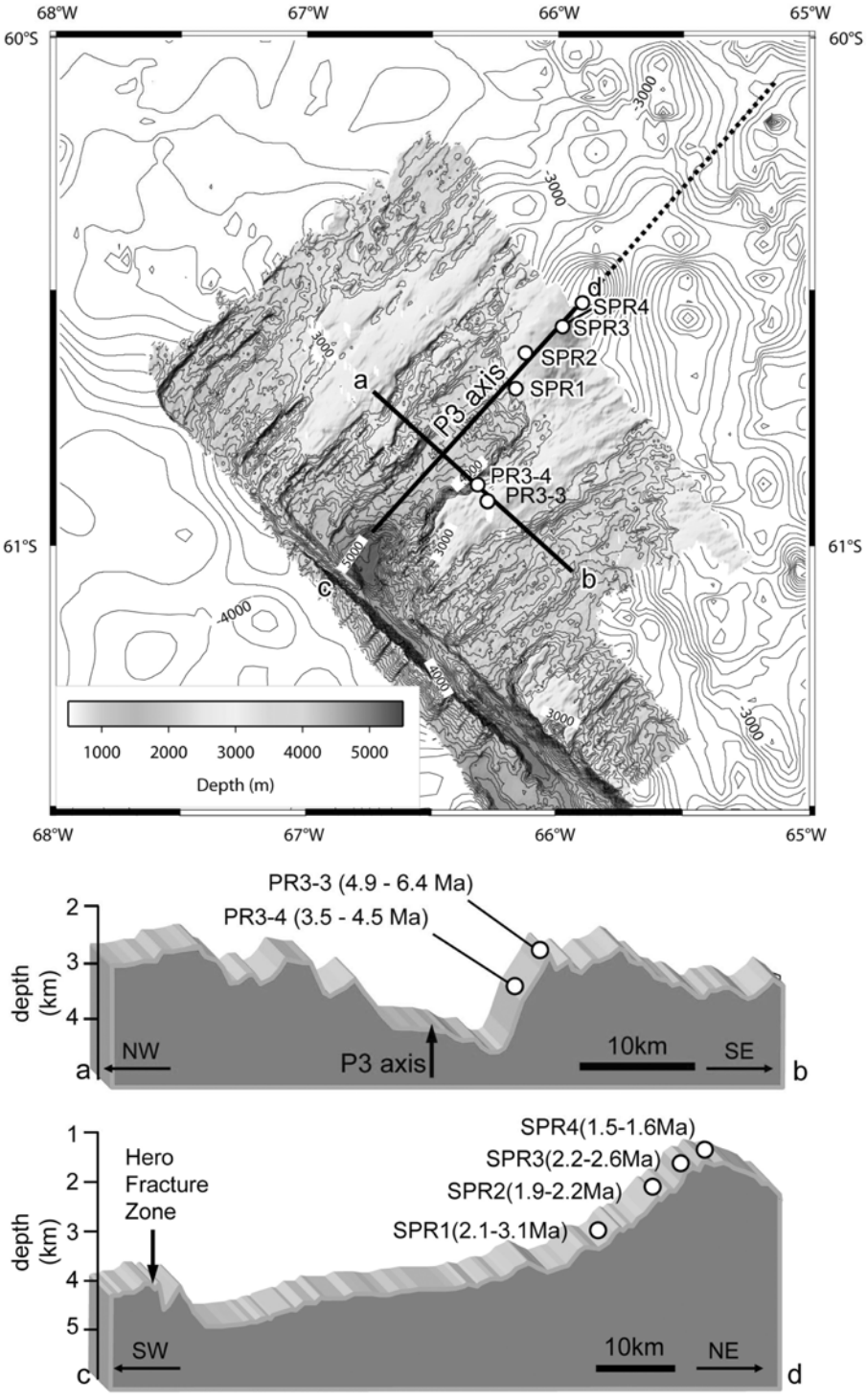

Fig. 3. Bathymetry and depth profile of the P3 segment, modified from Kim (2005). Circles represent sample locations and the K-Ar ages at these sites are shown in parentheses (Choe et al., 2005).

HFZ and runs over a distance of 200 km to northeast (Fig. 3). The near-axis morphology of the P3 segment also shows high relief. In the segment center, a prominent seamount is present, which rises 2,500 m from the axial valley floor at 4,000 m. The southwestern region of the axial seamount is flanked by two great ridges which rise to about 2,500 m depth. The northwestern flank is broader and further away from the ridge axis than the southeastern flank. It is supposed that both flanks may be the rifted parts of a former axial topographic high, and the different morphologies of the flanks may be caused by asymmetric lithospheric stretching during the final stage of extension (Kim, 2005). This suggestion is corroborated by magnetic anomalies, which show the difference of the spreading rates between the northwestern and southeastern flanks (Livermore et al., 2000).

The PR3 basalts were sampled from the two sites of steeper southeastern flank of the P3 segment. The K-Ar ages of these samples are 4.9-6.4 and 3.5-4.5 Ma, and also become younger toward the ridge axis (Choe et al., 2005). These ages are significantly older than those of the PR2 samples. The youngest K-Ar ages obtained from inner walls of the rifted ridges of the P2 and P3 segments probably represent or approximate the final extension stage. It is thus likely that extinction of spreading processes at the two segments occurred at different times: i.e., the spreading at the P3 segment terminated early. This temporal relationship is inconsistent with that of the geophysical investigation (Livermore et al., 2000).

The axial seamount occurs as a single volcano along the ridge axis of the P3 segment. It rises to a shallow 750 m depth and has a mean diameter of about 30 km. This kind of huge seamount, occurring at the ridge axis, is rare even in the slow-spreading ridges, not associated with hotspot volcanism (e.g., Northern Mid-Atlantic Ridge), which generally have low-relief axial highs (Perfit and Chadwick, Jr., 1998).

The K-Ar ages of axial seamount basalts (SPR), systematically collected with depth along the P3 axis (Fig. 3), range from 3.1 to 1.4 Ma, and become younger toward the top of the seamount, indicating a discrete, point-source eruption (Choe et al., 2005). In conjunction with the geophysical data (Livermore et al., 2000; Kim, 2005), the K-Ar ages suggest that huge axial seamount has formed after the extinction of spreading at the P3 segment.

4. SAMPLING AND ANALYTICAL METHODS

Submarine volcanic rocks of this study were obtained from 9 dredges on R/V *Yuzhmorgeologiya* during 2000-2001 and 2002-2003 summer cruises. Sample locations, together with K-Ar whole-rock ages, are shown in Figures 2 and 3. The PR2 basalts were dredged at depths of 2,400 m (PR2-2), 2,000 m (PR2-3), and 1,200 m (PR2-4) from the northwestern flank of the P2 segment, and the PR3 basalts were sampled at depths of 2,500 m (PR3-3) and 3,000 m (PR3-4) from the southeastern flank of the P3 segment. From the axial seamount of the P3 segment, the SPR samples were systematically collected at depths of 2,900 m (SPR1), 2,000 m (SPR2), and 1,000-800 m (SPR3 and SPR4).

The majority of samples are very fresh and many samples show pillow structures which have glassy surface and radial joints toward the outer margin. Major and trace element compositions for 44 samples were determined using an XRF (Philips, PW1480) and an ICP-MS (Perkin Elmer, Elan 6100) at Korea Polar Research Institute (KOPRI). Further analytical procedures are available in Lee (1994) and Hur et al. (2003).

5. RESULTS

The volcanic rocks from the APR show small variations in SiO_2 ranging from 49 to 52 wt%, MgO from 4 to 9 wt%, and Al_2O_3 from 15 to 18 wt% (Table 1). The PR3 basalts have the highest CaO, and the lowest K_2O, P_2O_5, Na_2O, TiO_2, and Al_2O_3 contents at a given MgO content (Fig. 4). The SPR basalts show a wide ranges of MgO, and can be divided into high (> 7 wt%) and low (< 7 wt%) MgO types. Na_2O, K_2O, P_2O_5, TiO_2, and Al_2O_3 in the SPR basalts increase with decreasing MgO. The concentrations of these elements systematically vary with the eruption ages of the SPR volcanics. The youngest one (SPR4) from the crest of the P3 axial seamount has the lowest MgO content. The PR2 volcanics have MgO contents less than 6.3 wt% (Table 1), and their compositional variations are generally similar to those of the low-MgO SPR basalts. However, the PR2 basalts show steeper variations of CaO and P_2O_5 compared to those of the low-MgO SPR basalts.

The APR basalts are divided into two magma types in the total alkali versus silica (TAS) diagram (Fig. 5). The PR3 volcanics (older than 3.5 Ma) with the lowest alkali contents belong to low-K tholeiities, whereas those from the PR2 and SPR (younger than 3.1 Ma) correspond to medium-K mildly alkaline basalts.

The Mg number ($Mg\# = 100\times Mg/(Mg + Fe^{2+})$) is generally higher in hotter, more primitive, and less-fractionated liquids. The PR2 and low-MgO SPR basalts have lower Mg numbers (< 60) (Fig. 6a). The Mg numbers of the PR3 and high-MgO SPR basalts are higher than 60, and their averages (64.3) are similar to the most primitive portion of the Mid-Atlantic Ridge basalts (63.9 ; Lehnert et al., 2000).

The large ion lithophile (LIL) elements are incompatible and enriched in E-MORB. Inter-element ratios of trace elements have been employed to distinguish different source reservoirs. The K/Ba ratio of N-MORB is commonly greater than 100, whereas that of E-MORB is lower than 30 (Morris and Hart, 1983). In the K/Ba vs. MgO plot (Fig. 6b), the PR3 basalts belong to N-MORB, while the PR2 and SPR basalts to E-MORB.

The APR basalts show large variations in incompatible element ratios. The La/Sm ratios of younger, PR2 and SPR basalts are higher (3.5-5.5) than those of the older PR3 basalts (< 1). The Zr/Y ratios vary from 4.7 to 12.4 for the younger basalts but almost constant (3-4) for the older ones (Fig. 6c). In particular, the Zr/Y ratios of the SPR basalts increase from 5 to 12.4, apparently with decreasing ages. These characteristics can not be attributed to fractional crystallization, but to different degree of mantle melting with or without contributions from different source materials. Sr is a key element for discriminating crystallization from melting process because it is compatible in plagioclase, and behaves compatibly during the crystallization but incompatibly during the mantle melting. The Sr contents vary little with decreasing MgO contents except for some high-MgO SPR basalts, and this behavior is observed for many MORB suites (Fig. 6d) (le Roux et al., 2002). The Sr vari-

Table 1. Major and trace element compositions of the Antarctic-Phoenix Ridge Basalts.

Sample	PR2 2-1	PR2 2-2	PR2 2-3	PR2 2-4	PR2 2-5	PR2 3-1	PR2 3-2	PR2 3-2G	PR2 3-3	PR2 3-3G	PR2 3-4	PR2 3-5	PR2 4-1	PR2 4-2	PR2 4-3	PR3 3-1
Major elements (in wt%)																
SiO_2	49.53	50.22	49.48	49.37	49.48	49.58	49.33	50.54	50.04	50.57	49.62	49.33	49.13	48.68	48.54	49.92
TiO_2	2.17	2.25	2.05	2.14	1.99	2.51	2.63	2.59	2.64	2.61	2.54	2.51	2.10	2.07	2.08	1.39
Al_2O_3	16.71	16.42	16.74	16.06	17.18	16.46	16.41	16.31	16.47	16.26	16.84	16.77	16.50	15.76	15.90	15.04
FeO*	9.15	9.35	9.09	10.26	8.72	10.09	10.06	9.91	10.03	9.82	9.98	9.84	10.37	10.49	10.57	9.02
MnO	0.16	0.18	0.16	0.18	0.15	0.18	0.16	0.17	0.17	0.17	0.17	0.16	0.19	0.17	0.21	0.16
MgO	5.11	5.36	5.83	6.23	5.73	4.57	4.53	5.31	4.45	5.04	4.34	4.72	5.78	5.87	5.63	7.45
CaO	9.77	8.86	10.29	10.67	10.49	8.74	9.08	8.88	8.81	8.56	9.05	9.44	10.90	10.34	10.44	12.17
Na_2O	3.45	3.66	3.32	3.07	3.25	3.71	3.56	3.74	3.64	3.82	3.62	3.46	3.00	2.99	3.03	2.74
K_2O	1.42	1.66	1.26	1.01	1.21	1.58	1.40	1.30	1.56	1.41	1.50	1.43	0.93	1.00	0.96	0.29
P_2O_5	0.53	0.64	0.47	0.37	0.45	0.63	0.57	0.56	0.61	0.61	0.64	0.57	0.35	0.36	0.37	0.13
LOI	1.32	1.02	0.87	0.29	0.88	1.32	1.54	0.75	1.48	0.62	1.18	1.23	0.62	1.32	1.02	0.72
Total	99.35	99.60	99.55	99.65	99.54	99.37	99.28	100.06	99.92	99.47	99.47	99.45	99.87	99.06	98.74	99.02
Mg#	52.52	53.16	55.97	54.62	56.54	47.28	47.12	51.50	46.77	50.44	46.25	48.73	52.46	52.58	51.35	62.07
Trace elements (in ppm)																
Be	1.5	1.8	1.5	1.3	1.5	1.9	1.7	1.8	1.9	2.5	2.0	1.9	1.3	1.4	1.3	0.5
Li	10.1	10.1	10.3	8.6	10.4	12.0	11.0	8.9	10.1	9.2	12.9	11.8	12.8	12.3	14.0	4.8
Sc	35.4	31.3	36.6	38.4	34.9	34.4	36.0	36.0	34.2	35.2	34.3	35.5	41.4	41.5	42.9	42.2
Co	37.5	34.7	38.3	44.1	36.6	34.9	36.6	37.8	34.8	36.3	34.8	37.8	51.9	48.6	57.6	43.8
Cr	172.5	168.0	204.7	148.8	227.5	110.1	70.5	72.9	64.5	66.6	110.3	129.4	138.7	130.1	135.6	341.4
Cu	69.8	68.3	71.7	78.4	70.2	55.7	57.4	55.2	56.0	55.3	54.9	62.2	75.1	73.8	77.5	74.9
Zn	96.7	109.6	100.3	99.3	96.8	109.5	101.1	88.3		90.3	112.5	105.1	108.5	112.8	114.7	65.3
Mo	2.8	3.5	2.5	1.9	2.4	3.3	2.9	3.1	3.1	3.3	3.0	3.0	2.5	1.9	2.6	0.3
Ni	70.4	74.9	82.2	61.0	82.3	52.3	52.5	60.3	48.9	56.6	53.6	66.3	78.0	64.4	72.3	71.7
Cs	0.4	0.4	0.3	0.2	0.2	0.3	0.3	0.3	0.3	0.3	0.3	0.3	0.2	0.2	0.2	0.3
V	332.9	323.2	320.7	358.1	312.9	359.7	393.1	390.8	386.6	396.8	371.3	384.8	377.7	390.4	402.8	289.7
Ga	22.9	24.1	21.9	20.8	21.7	24.2	24.8	24.2	24.8	24.9	24.7	25.1	22.2	21.8	22.3	16.5
Rb	22.0	33.1	22.4	18.7	22.3	27.5	24.6	30.7	27.0	33.1	24.1	26.7	17.5	17.4	17.4	6.2
Sr	309.3	302.2	312.8	317.4	310.9	315.2	337.3	321.2	325.4	321.9	317.6	334.9	337.8	334.7	341.1	165.9
Y	44.7	50.7	40.9	35.0	38.5	52.1	48.8	48.8	49.3	51.1	51.4	48.3	37.2	37.2	38.1	27.4
Zr	239.6	288.2	222.2	171.9	210.4	288.5	274.3	277.0	293.2	297.9	286.1	270.6	175.4	176.5	178.2	97.3
Nb	48.1	60.0	44.0	34.1	41.6	57.5	52.9	52.0	55.8	55.5	55.4	52.0	32.9	33.5	32.9	2.7
Ta	2.9	3.6	2.7	2.1	2.5	3.5	3.3	3.1	3.3	3.3	3.4	3.1	2.0	2.0	2.0	0.2
Hf	5.6	6.4	5.1	4.2	4.8	6.4	6.3	6.1	6.4	6.4	6.3	6.0	4.1	4.1	4.3	2.7
Ba	287.0	365.3	270.3	221.0	243.6	337.7	315.4	315.8	328.0	331.2	327.4	296.2	211.4	211.6	216.3	9.2
U	1.1	1.4	1.0	0.7	0.9	1.3	1.1	1.2	1.2	1.3	1.3	1.2	0.7	0.7	0.8	0.1
Th	3.7	4.7	3.3	2.4	3.2	4.5	4.1	4.1	4.3	4.4	4.6	4.1	2.4	2.5	2.5	0.2
La	31.3	39.3	29.2	22.5	26.6	37.4	34.1	33.8	35.6	36.3	36.3	32.5	21.9	21.9	22.6	4.0
Ce	63.4	79.6	58.2	45.7	54.2	75.7	70.3	71.3	74.5	75.6	74.2	67.6	43.6	44.0	44.6	12.3
Pr	7.3	8.9	6.8	5.3	6.3	8.6	8.1	8.0	8.5	8.4	8.5	7.8	5.2	5.3	5.4	2.0
Nd	30.9	37.0	28.9	23.0	26.5	36.6	35.0	34.1	36.1	36.0	36.1	33.4	23.1	23.1	23.6	10.4
Sm	8.9	8.4	6.5	5.4	6.2	8.3	7.8	7.9	8.2	8.3	8.2	7.7	5.6	5.6	5.7	3.5
Eu	2.3	2.6	2.1	1.9	2.0	2.6	2.5	2.5	2.5	2.6	2.6	2.4	1.9	1.9	2.0	1.3
Gd	7.6	8.6	7.2	6.0	6.9	8.9	8.6	8.5	8.6	8.7	8.8	8.6	6.4	6.5	6.6	4.5
Tb	1.3	1.5	1.2	1.0	1.1	1.5	1.4	1.4	1.4	1.5	1.5	1.4	1.1	1.1	1.1	0.8
Dy	7.6	8.8	7.0	6.1	6.8	8.9	8.5	8.5	8.8	8.8	8.6	8.4	6.3	6.3	6.4	5.1
Ho	1.6	1.8	1.5	1.2	1.4	1.8	1.8	1.7	1.8	1.8	1.8	1.7	1.3	1.3	1.3	1.1
Er	4.7	5.2	4.3	3.6	4.0	5.4	5.1	5.1	5.2	5.3	5.3	5.0	3.8	3.9	4.0	3.1
Tm	0.7	0.8	0.6	0.5	0.6	0.8	0.8	0.8	0.8	0.8	0.8	0.8	0.6	0.6	0.6	0.5
Yb	4.1	4.8	3.8	3.3	3.7	4.9	4.6	4.6	4.8	4.8	4.8	4.6	3.5	3.5	3.5	2.9
Lu	0.7	0.7	0.6	0.5	0.6	0.8	0.7	0.7	0.7	0.7	0.8	0.7	0.5	0.5	0.6	0.4

*Total Fe as FeO. Mg#, 100xMg/(Mg+Fe^{2+}) in mole.

G, glass; PR2, P2 segment; PR3, P3 segment; SPR, axial seamount in the P3 segment.

Table 1. (continued)

Sample	PR3 3-2	PR3 3-3G	PR3 3-4	PR3 3-5	PR3 4-2	PR3 4-3	PR3 4-4	SPR1 1	SPR1 2	SPR1 2G	SPR1 3	SPR1 3G	SPR2 1G	SPR2 2	SPR2 3	SPR2 4
Major elements (in wt%)																
SiO_2	50.82	50.65	50.29	50.43	49.02	49.09	49.95	48.81	48.55	49.29	48.50	49.47	48.78	48.51	48.46	48.47
TiO_2	1.43	1.40	1.41	1.43	1.23	1.25	1.25	1.60	1.60	1.59	1.59	1.58	1.91	1.93	1.88	1.89
Al_2O_3	15.32	15.17	15.14	15.25	16.82	16.94	17.02	16.60	16.63	16.20	16.55	16.36	16.70	16.70	16.64	16.83
FeO*	8.80	8.92	8.75	8.67	8.91	8.92	8.69	8.32	8.44	8.22	8.27	8.05	8.43	8.66	8.64	8.69
MnO	0.16	0.17	0.16	0.16	0.15	0.15	0.15	0.15	0.15	0.15	0.15	0.15	0.15	0.15	0.15	0.16
MgO	7.44	8.14	7.53	7.12	7.55	7.09	7.91	8.43	8.45	9.00	8.41	8.94	7.70	7.07	7.42	7.21
CaO	12.03	11.95	11.89	11.99	12.12	12.07	12.21	10.90	11.02	10.88	10.85	10.82	10.48	10.40	10.41	10.47
Na_2O	2.76	2.85	2.77	2.77	2.60	2.60	2.55	2.86	2.87	2.84	2.85	2.86	3.27	3.20	3.26	3.21
K_2O	0.35	0.14	0.26	0.40	0.17	0.15	0.26	0.68	0.63	0.68	0.71	0.66	1.16	1.31	1.23	1.23
P_2O_5	0.13	0.13	0.14	0.14	0.12	0.13	0.11	0.31	0.31	0.31	0.32	0.30	0.46	0.45	0.45	0.45
LOI	0.41	0.28	0.55	1.26	0.39	0.82	0.93	0.66	0.87	0.23	1.31	0.25	0.23	1.20	0.80	0.85
Total	99.66	99.79	98.89	99.61	99.06	99.21	101.02	99.32	99.52	99.39	99.51	99.44	99.27	99.60	99.34	99.45
Mg#	62.62	64.39	63.03	61.93	62.67	61.18	64.33	66.76	66.47	68.44	66.82	68.76	64.41	61.79	63.00	62.16
Trace elements (in ppm)																
Be	0.5	0.5	0.5	0.5	0.4	0.4	0.4	1.0	1.0	1.0	1.0	1.1	1.4	1.5	1.5	1.6
Li	5.6	5.2	5.2	5.3	8.8	13.2	6.0	7.2	8.4	6.7	7.9	6.7	6.9	8.3	6.8	8.9
Sc	41.9	42.6	45.6	42.8	37.4	37.7	37.0	34.4	35.2	35.4	35.9	35.9	36.1	37.0	35.8	37.4
Co	43.7	47.2	47.9	48.2	44.6	44.6	47.1	45.4	45.5	48.0	45.8	47.9	44.7	45.0	44.7	47.5
Cr	345.6	340.8	360.7	350.0	359.1	343.5	366.7	446.3	439.2	459.5	446.2	472.8	212.1	211.7	214.7	217.8
Cu	75.3	77.7	79.7	76.2	76.2	80.5	73.7	60.3	64.1	64.8	61.4	65.3	63.8	61.6	60.4	61.5
Zn	66.1	64.0	68.3	67.8	86.6	91.6	69.4	74.2	71.7	59.8	73.7	57.7	60.9	72.1	69.5	78.3
Mo	0.3	0.5	0.4	0.5	0.3	0.3	0.3	1.3	1.2	1.6	1.3	1.6	2.7	2.6	2.2	2.3
Ni	70.5	76.5	77.4	75.8	105.9	107.2	117.6	190.9	193.9	206.7	196.1	204.8	135.4	127.7	142.3	153.5
Cs	0.4	0.0	0.2	0.4	0.2	0.0	0.2	0.1	0.1	0.2	0.1	0.2	0.3	0.3	0.3	0.3
V	281.0	279.1	299.4	285.4	271.9	278.0	260.7	296.0	303.1	308.7	307.5	300.2	313.3	343.7	323.8	334.8
Ga	16.6	16.3	17.4	16.8	17.4	17.2	17.1	18.6	18.6	18.3	18.2	18.1	19.4	19.6	19.7	19.8
Rb	8.2	1.2	5.6	9.4	2.4	1.5	4.6	11.3	9.9	14.5	11.1	14.5	25.7	19.3	16.6	16.2
Sr	174.3	167.2	177.9	172.3	150.0	153.6	148.0	279.0	281.2	268.3	275.6	269.4	361.5	369.5	371.2	375.5
Y	27.3	27.0	28.8	27.2	25.4	26.2	24.9	28.1	28.1	27.7	28.6	27.1	27.4	29.4	28.0	28.7
Zr	95.5	96.0	101.5	96.6	77.5	78.5	76.2	133.9	136.3	136.7	136.8	134.8	183.9	187.8	184.2	186.3
Nb	2.8	3.0	2.9	2.9	2.8	2.8	2.8	27.0	26.8	26.2	26.5	26.2	46.5	47.6	46.6	46.2
Ta	0.3	0.3	0.2	0.3	0.3	0.2	0.2	1.6	1.7	1.6	1.6	1.6	3.2	2.8	2.9	2.8
Hf	2.6	2.6	2.7	2.7	2.1	2.2	2.2	3.5	3.5	3.6	3.4	3.6	4.1	4.1	4.1	4.2
Ba	9.8	9.8	9.8	13.7	13.7	14.5	9.1	150.7	143.5	161.7	147.8	164.2	259.3	264.1	256.9	258.5
U	0.1	0.1	0.1	0.1	0.1	0.1	0.1	0.6	0.5	0.7	0.6	0.7	1.2	1.2	1.1	1.2
Th	0.2	0.3	0.3	0.3	0.3	0.2	0.2	2.2	2.3	2.3	2.3	2.3	4.0	4.1	4.0	4.1
La	3.9	4.2	4.2	4.2	3.5	3.4	3.2	17.1	16.8	16.9	17.0	16.6	25.4	26.9	25.4	25.7
Ce	12.1	13.1	12.9	12.7	9.7	9.9	9.5	35.9	36.2	36.8	36.3	36.2	50.7	53.9	51.7	51.4
Pr	2.0	2.1	2.1	2.1	1.7	1.6	1.6	4.7	4.7	4.6	4.7	4.6	6.1	6.3	6.2	6.3
Nd	10.6	10.8	11.2	10.8	8.6	8.6	8.4	19.9	20.1	19.5	19.9	19.8	24.7	25.3	24.6	25.4
Sm	3.5	3.5	3.6	3.5	3.0	3.0	2.8	4.9	4.9	4.8	4.9	4.7	5.5	5.7	5.5	5.5
Eu	1.4	1.4	1.4	1.4	1.2	1.2	1.1	1.7	1.7	1.7	1.7	1.7	1.8	1.9	1.9	1.9
Gd	4.6	4.6	4.9	4.7	4.0	4.0	4.0	5.5	5.4	5.2	5.5	5.2	5.8	5.6	5.6	5.8
Tb	0.8	0.8	0.9	0.8	0.7	0.7	0.7	0.9	0.9	0.9	0.9	0.9	0.9	1.0	0.9	1.0
Dy	5.0	5.1	5.3	5.1	4.7	4.8	4.6	5.5	5.5	5.4	5.6	5.4	5.5	5.7	5.6	5.8
Ho	1.1	1.1	1.1	1.1	1.0	1.0	1.0	1.2	1.1	1.1	1.2	1.1	1.2	1.2	1.2	1.2
Er	3.1	3.2	3.3	3.2	3.0	3.0	2.9	3.3	3.3	3.3	3.3	3.2	3.2	3.4	3.3	3.4
Tm	0.5	0.5	0.5	0.5	0.4	0.5	0.4	0.5	0.5	0.5	0.5	0.5	0.5	0.5	0.5	0.5
Yb	2.9	2.8	3.1	2.9	2.8	2.8	2.7	3.0	3.0	2.9	3.0	3.0	2.9	3.0	2.9	3.1
Lu	0.5	0.5	0.5	0.5	0.4	0.4	0.4	0.5	0.5	0.5	0.5	0.5	0.5	0.5	0.5	0.5

Table 1. (continued)

Sample	SPR3 1	SPR3 2	SPR3 3	SPR3 4	SPR4 1	SPR4 2	SPR4 3	SPR4 4	SPR4 5	SPR4 6	SPR4 7	SPR4 8
Major elements (in wt%)												
SiO_2	50.80	49.89	50.50	49.97	50.98	50.38	51.49	51.85	51.73	51.38	50.29	50.82
TiO_2	2.47	2.48	2.35	2.39	2.22	2.43	2.43	2.42	2.39	2.54	2.50	2.36
Al_2O_3	16.45	16.73	16.72	16.98	17.55	17.41	17.80	17.85	17.68	17.68	17.40	17.25
FeO*	9.82	9.68	9.40	9.45	8.44	8.90	8.63	8.58	8.54	8.99	8.97	8.48
MnO	0.20	0.26	0.19	0.21	0.15	0.20	0.17	0.15	0.15	0.16	0.18	0.16
MgO	5.95	5.69	6.01	6.06	6.00	5.53	4.50	4.92	4.89	4.37	4.52	5.54
CaO	9.92	9.94	9.77	10.03	9.32	9.49	9.57	9.52	9.43	9.68	9.66	9.34
Na_2O	3.24	3.15	3.20	3.16	3.59	3.52	3.83	3.73	3.89	3.82	3.60	3.68
K_2O	1.15	1.02	1.10	0.95	1.45	1.38	1.55	1.59	1.56	1.60	1.47	1.42
P_2O_5	0.42	0.45	0.41	0.33	0.43	0.50	0.47	0.33	0.36	0.57	0.51	0.45
LOI	0.21	1.15	0.4	0.32	0.35	0.78	0.25	0.21	0.31	0.27	1.2	0.68
Total	100.63	100.45	100.04	99.84	100.49	100.50	100.68	101.13	100.92	101.05	100.31	100.17
Mg#	54.54	53.78	55.86	55.94	58.47	55.17	50.81	53.16	53.16	49.02	49.98	56.44
Trace elements (in ppm)												
Be	1.0	1.0	1.0	0.9	1.0	1.1	0.9	1.0	1.1	1.1	1.1	1.1
Li	6.3	6.9	6.1	6.1	6.8	6.4	6.5	5.8	6.7	6.7	6.7	6.5
Sc	28.1	28.8	27.5	27.5	22.3	23.4	24.4	23.2	23.5	22.6	23.4	23.3
Co	37.7	60.9	39.9	48.4	28.9	41.9	34.6	24.0	23.5	25.4	34.3	29.3
Cr	186.8	183.5	189.7	196.2	99.6	89.3	88.5	96.1	96.0	89.7	91.3	95.7
Cu	50.2	47.5	43.6	38.9	49.4	44.0	36.7	37.9	38.1	54.8	45.0	44.1
Zn	119.6	133.1	116.6	119.8	99.7	111.7	106.3	92.4	97.0	104.1	105.6	101.2
Mo	2.8	2.9	2.9	2.7	2.9	3.2	1.7	2.5	2.1	2.8	2.7	3.2
Ni	86.4	90.7	91.4	98.7	67.0	59.8	45.7	45.7	46.3	39.8	47.0	53.9
Cs	0.2	0.2	0.2	0.2	0.3	0.2	0.1	0.2	0.1	0.2	0.1	0.2
V	323.1	333.8	320.0	326.6	235.7	262.4	290.5	274.1	271.3	291.6	282.1	274.2
Ga	20.7	21.0	20.7	20.4	17.8	18.6	18.9	18.8	18.5	18.9	18.2	18.3
Rb	16.8	14.1	15.7	12.8	23.9	20.9	22.8	22.3	23.3	10.9	18.9	21.0
Sr	258.6	273.0	265.1	271.1	394.4	395.6	387.4	383.2	387.8	382.3	385.8	391.2
Y	30.3	32.5	29.8	25.8	21.2	26.4	22.2	18.9	18.1	24.2	24.7	24.4
Zr	214.0	220.1	213.8	198.7	204.5	224.3	212.0	217.4	224.4	231.5	221.5	227.5
Nb	40.1	41.9	40.2	39.3	51.0	54.1	54.5	53.4	54.2	56.3	54.2	54.4
Ta	4.2	3.9	3.5	3.3	4.3	4.5	4.4	4.4	4.5	4.7	4.6	4.6
Hf	5.3	5.6	5.4	5.2	5.0	5.7	5.7	5.6	5.8	6.0	5.9	6.0
Ba	191.9	192.3	187.8	176.4	311.8	312.7	333.6	322.1	332.2	334.3	329.9	323.1
U	0.8	0.9	0.8	0.7	1.0	1.6	0.9	0.9	1.0	1.4	1.2	1.1
Th	2.6	3.4	2.7	2.8	4.0	4.7	4.4	3.5	3.9	4.3	4.7	4.4
La	18.6	20.7	18.1	14.5	21.4	25.8	18.3	14.4	13.9	20.5	22.4	22.9
Ce	39.5	48.4	38.4	33.9	41.4	51.6	41.5	29.7	28.6	43.5	46.4	45.0
Pr	4.7	5.2	4.6	3.8	4.7	5.9	4.6	3.6	3.6	5.1	5.3	5.2
Nd	19.8	21.8	19.3	16.3	18.5	23.1	18.8	14.8	14.9	21.2	21.8	20.8
Sm	4.9	5.3	4.8	4.2	4.0	5.2	4.4	3.5	3.5	4.9	5.0	4.7
Eu	1.8	1.9	1.7	1.6	1.5	1.8	1.7	1.5	1.5	1.8	1.8	1.7
Gd	6.1	6.6	6.1	5.3	4.8	6.2	5.3	4.3	4.3	5.9	6.0	5.7
Tb	1.0	1.1	1.0	0.9	0.7	0.9	0.8	0.7	0.7	0.9	0.9	0.9
Dy	6.0	6.5	6.0	5.2	4.3	5.5	4.8	4.0	4.0	5.4	5.4	5.2
Ho	1.2	1.3	1.2	1.1	0.9	1.1	0.9	0.8	0.8	1.1	1.1	1.0
Er	3.5	3.8	3.5	3.1	2.5	3.2	2.7	2.4	2.3	3.1	3.1	3.0
Tm	0.6	0.6	0.6	0.5	0.4	0.5	0.4	0.4	0.4	0.5	0.5	0.5
Yb	3.4	3.6	3.3	3.0	2.5	3.1	2.7	2.4	2.4	3.0	2.9	3.0
Lu	0.5	0.5	0.5	0.5	0.4	0.5	0.4	0.4	0.4	0.4	0.4	0.4

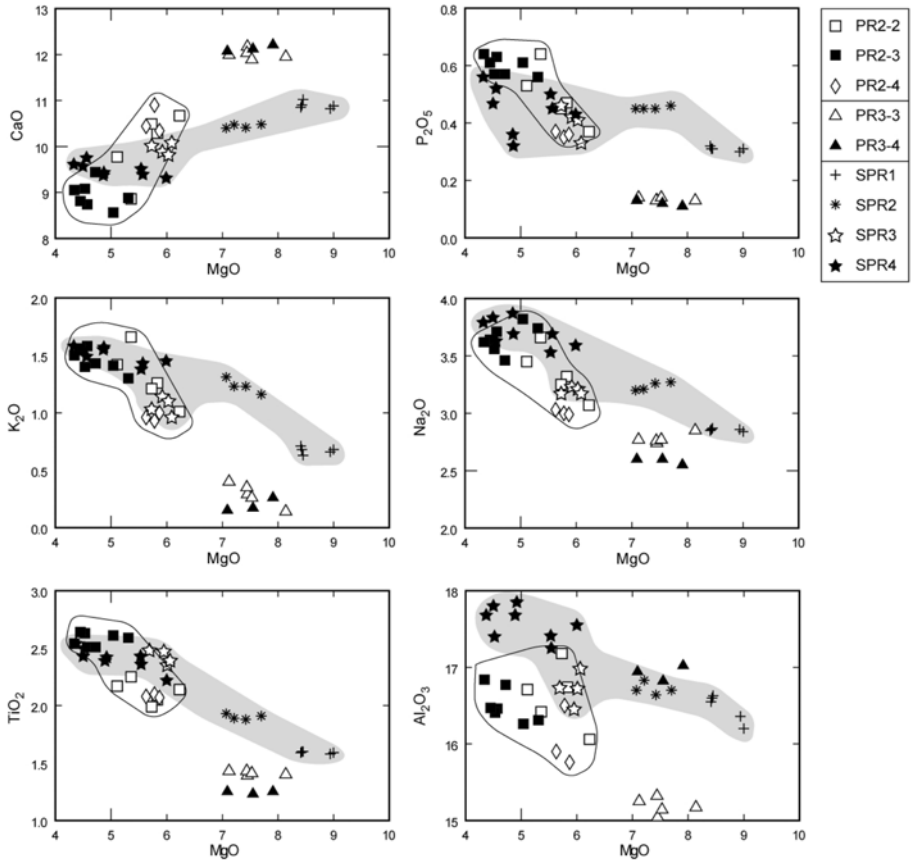

Fig. 4. CaO, P_2O_5, K_2O, Na_2O, TiO_2, and Al_2O_3 vs. MgO variation diagrams. Abbreviations: PR2, P2 segment; PR3, P3 segment; SPR, seamount of P3 segment.

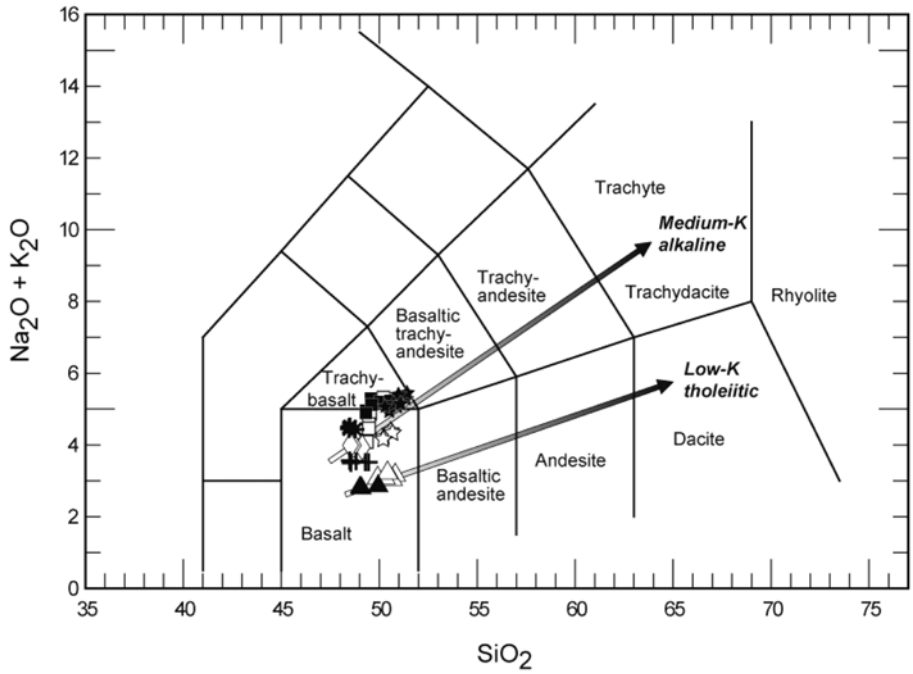

Fig. 5. Classification and nomenclature of the APR basalts using the Total alkali-silica (TAS) diagram of Le Maitre et al. (1989). Symbols are the same as Figure 4.

ations of the APR basalts are thus considered to reflect those of mantle sources.

The sodium behaves as a moderately incompatible element, and its concentration in melt is roughly inversely proportional to the extent of melting. Liquid lines of descent from each area can be calculated for low-pressure fractionation of olivine, plagioclase and clinopyroxene from primary magma. Because these lines are subparallel, the Na_2O content at 8 wt % MgO ($Na_{8.0}$) can be inferred by projecting along a line. The $Na_{8.0}$ approximates the sodium abundance

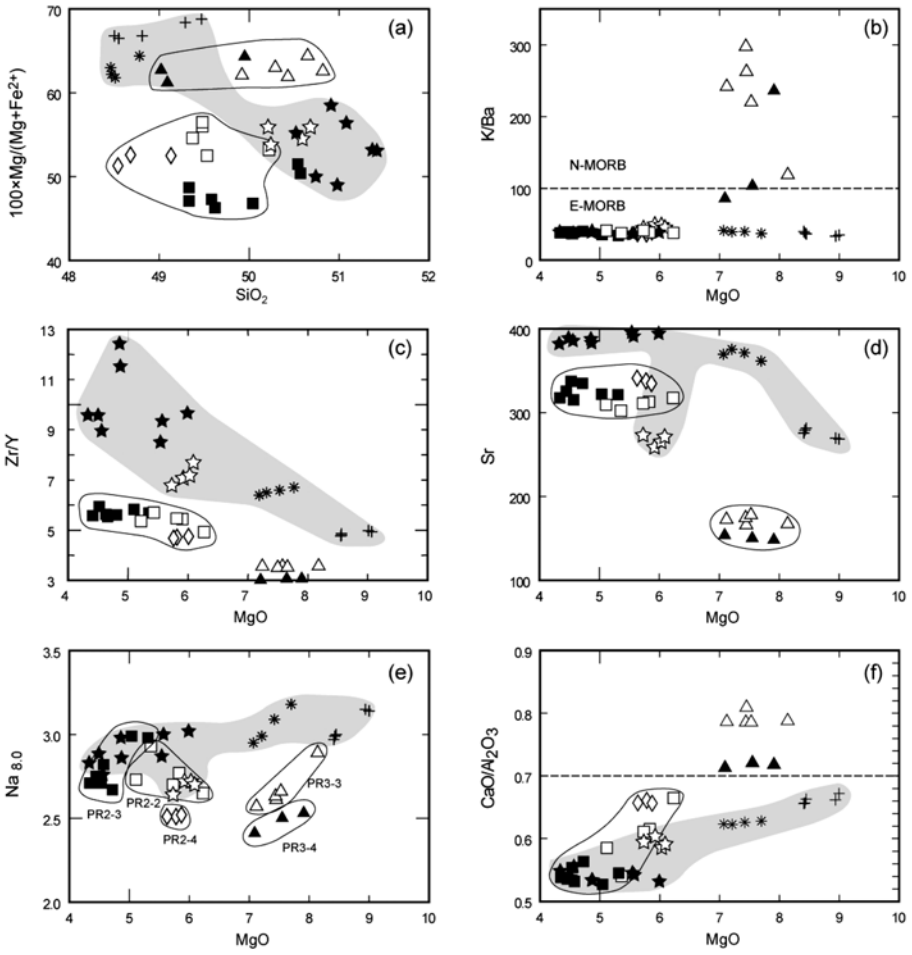

Fig. 6. (a) Mg# versus SiO_2 for the APR basalts. Fe^{2+} was calculated 0.9 x total Fe. (b) K/Ba versus MgO, (c) Zr/Y versus MgO, (d) Sr versus MgO, (e) $Na_{8.0}$ versus MgO, and (f) CaO/Al_2O_3 versus MgO plots for the APR basalts. The K/Ba ratios demonstrate that basalts from the PR3 have the signature of N-type MORB, and those from the PR2 and SPR belong to the E-type MORB. Symbols are the same as Figure 4.

in relatively primitive magma and regional Na variations indicate the change in the degree of melting (Klein and Langmuir, 1987). The extent of melting is thus likely to be lower in the mantle source of the younger, E-type basalts (PR2 and SPR) than in that of the older, N-type basalts (PR3) (Fig. 6e).

In general, Ca increases and Al decreases in melts with the progression of melting, compared to the Na variability, because Ca and Al are major components of mantle materials (Niu and Hékinian, 1997). In particular, the Ca/Al ratio increases nearly linearly with melting until clinopyroxene is exhausted at the condition of high (>25%) degree of melting (Jaques and Green, 1980; Niu and Batiza, 1991). The CaO/Al_2O_3 ratios of the PR3 basalts are higher than 0.7, and those of the PR2 and SPR basalts lower than 0.7, indicating that the former represents higher degree of melting than the latter (Fig. 6f).

The CaO/Al_2O_3 ratios from the E-type PR2 and SPR basalts gradually decrease with decreasing MgO, toward younger varieties. These correlations clearly support the assumption that the extent of melting gradually decreased with time during the generation of the younger, E-type basalts.

N-MORB normalized multi-element diagrams also show different patterns between the older and younger basalts (Fig. 7). The older PR3 basalts generally show similar patterns to those of N-MORB, but are much higher in some of incompatible elements, such as Cs, Rb, and K, compared to those in typical N-MORB (Fig. 7a). This apparent inconsistency is attributed to alteration because the altered MORB are strongly enriched in Cs (65x higher than fresh glass), Rb and U (both ~10x higher than glass) (Krolikowska-Ciaglo et al., 2003). Wei et al., (2004) reported that the alkali metals (K, Rb, Cs) are strongly partitioned into the fluid phase at high temperatures. Thus, ridge-crest hydrothermal fluid from younger E-type MORB may have affected the older N-type MORB. In addition, the extent of enrichment in the PR3 basalts increases, slightly but progressively, toward more incompatible elements. This feature may indicate that the enriched component was contributed to the mantle source or the melting degree was lower than that of N-MORB during the formation of primary magma for the PR3 basalts.

The younger PR2 and SPR basalts are highly enriched, corresponding to that of E-MORB (Fig. 7b). They are enriched in the incompatible elements, such as Rb, Ba, Th, U, Nb, and LREE, and the extent of enrichment progressively decreases toward more compatible elements. However, it is

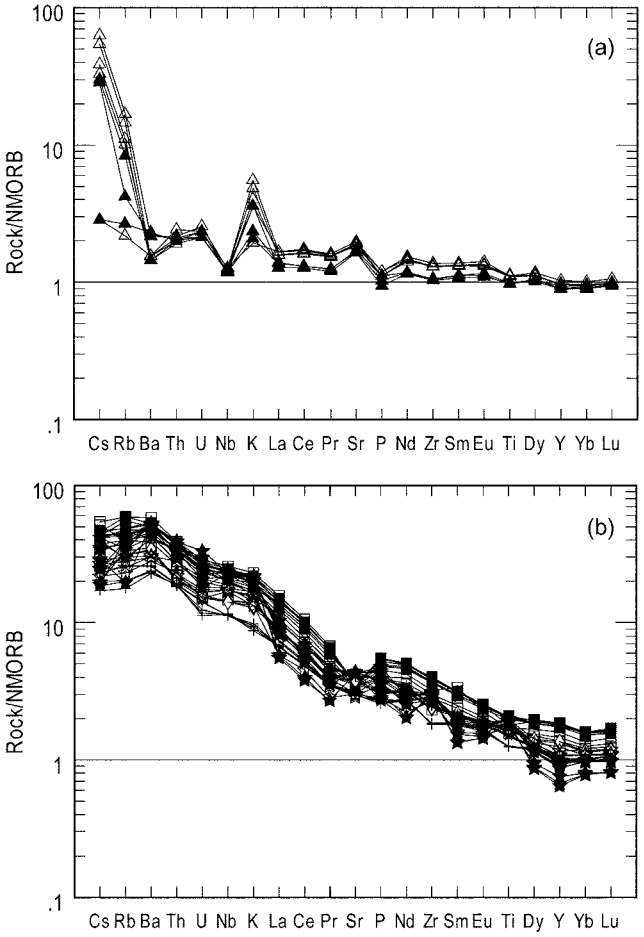

Fig. 7. N-MORB normalized trace element patterns of (a) PR3 basalts and (b) PR2 and SPR basalts. Symbols are the same as Figure 4. The N-MORB data used in the normalization are from Sun and McDonough (1989).

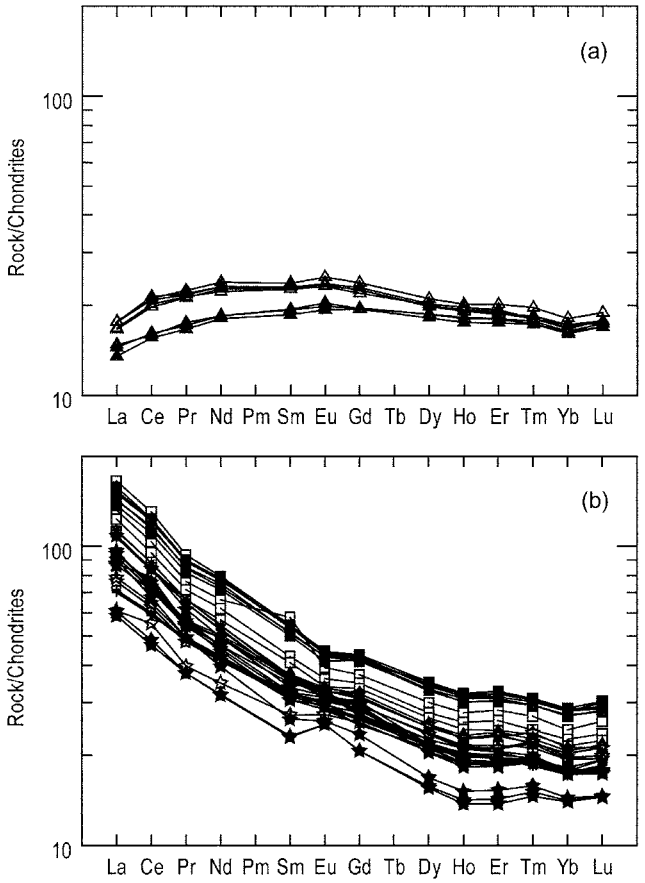

Fig. 8. Chondrite-normalized REE patterns of (a) PR3 basalts and (b) PR2 and SPR basalts. Symbols are the same as Figure 4. The chondritic values used for the REE normalization are from Sun and McDonough (1989).

difficult to change drastically from N-MORB to E-MORB environments during a short time interval of about 0.5 m.yr., if the mantle source is homogeneous. There is currently no direct evidence for the presence of heterogeneous enriched mantle, such as metasomatized mantle veins, beneath the APR. If veins are present, the E-type signatures of the younger PR2 and SPR basalts can be explained by lower extent of mantle melting, because mantle veins would preferentially participate in the melting at low-temperature and low-extent melting regime (Holness and Richter, 1989; Hirschmann and Stolper, 1996).

The REE patterns are basically consistent with trace element patterns. On the chondrite-normalized REE plots, the older PR3 basalts exhibit overall flat patterns with slight depletion in LREE (Fig. 8a), indicating that garnet is unlikely to be a residual phase during the melting, whereas the younger PR2 and SPR basalts show LREE-enriched patterns relative to HREE, suggesting a small degree of partial melting and/or a possible presence of garnet in the sources (Fig. 8b).

6. DISCUSSION AND CONCLUSIONS

6.1. Occurrence of E-MORB in a Fossil Ridge System

The enriched chemistry of E-MORB has been commonly explained by influence of hotspots or plumes, because plumes can impose large physical and chemical anomalies on normal ridges, such as variation of mantle flow, melting, axial morphology, and basalts chemistry (Rhodes et al., 1990; Douglass et al., 1999). However, the APR area is situated far away from any hotspot. Donnelly et al. (2000) revealed that a small proportion of basalt (E-MORB) is enriched in incompatible elements from the Mid-Atlantic Ridge, south of the Kane Fracture Zone. It is apparent that the enriched magma sources, not associated with hotspots, are widespread in the upper mantle and are common on both fast- and slow-spreading ridges (Cooper et al., 2004; Donnelly et al., 2004).

Alternatively, the occurrence of E-MORB may be related to the abrupt reduction in spreading rates and/or the extinction of spreading. This reduction results in a temporary

magma oversupply, leading to high extrusion rate and high volcanic edifice (Mitchell and Livermore, 1998). In the APR, extinction appears to have been simultaneous on all three segments at the magnetic chron of C2A (3.3 Ma; Livermore et al., 2000). This result together with K-Ar age data (Choe et al., 2005) suggest that the magmas to form SPR (3.1-1.5 Ma) and PR2 (2.1-1.4 Ma) volcanics, with E-MORB signatures, are supplied after the cessation of spreading.

Processes of melt segregation in the mantle can lead to discrete loci of melt delivery, and melt focusing can occur in the absence of tectonic influences (Whitehead et al., 1984). The ultraslow-spreading at PR3 prior to extinction may foster the focusing of partial melts, and consequently a large seamount (SPR) after the extinction of spreading. The upward younging trend in the flank of this seamount (Fig. 3) clearly supports this possibility. At PR2, however, the same process would have happened at the former rifted fault in northwest rather than the central axis (Fig. 2).

6.2. Origin of E-MORB at the APR

The rapid change from N-MORB to E-MORB in the APR could be attributed to the increase in lithospheric thickness with time and consequently in the contribution of enriched melt to N-MORB, together with the decrease in the degree of partial melting. Because $(Sm/Yb)_N$ is sensitive to final depth of melting (Shen and Forsyth, 1995), the higher $(Sm/Yb)_N$ ratios of E-MORB at the APR (1.5~2.2) indicate deeper final depths of melting than those of N-MORB (1.2~1.4). As the spreading rate decreases and ultimately becomes zero, the extent of mantle melting and melting column (solidus to liquidus depth interval) would decrease due to conductive cooling and lithospheric thickening. The low degree of melting in the mantle, responsible for the formation of E-MORB beneath the APR, may reflect either an abrupt change of tectonic process or an extinction of spreading. However, the latter alone cannot explain geochemical characteristics of the APR basalts.

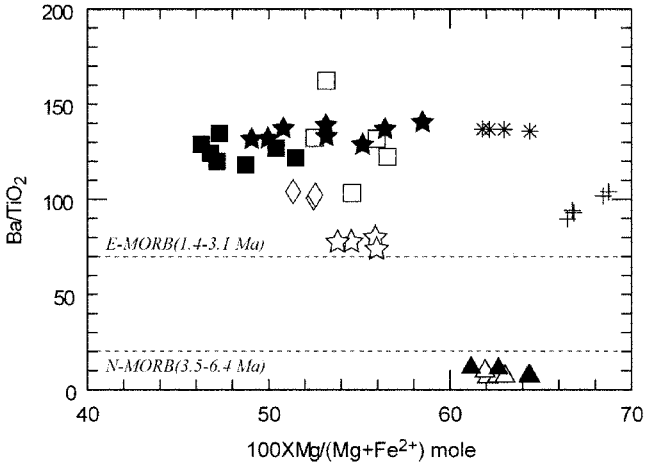

Fig. 9. Ba/TiO_2 vs. Mg# plot of the APR basalts. Note that the younger SPR and PR2 basalts have higher Ba/TiO_2 ratios (>70), indicating an enrichment of mantle source prior to eruption. Symbols are the same as Figure 4.

The Ba/TiO_2 ratio is a key index for evaluating an enrichment of mantle sources in incompatible elements (Michael et al., 2003). The SPR and PR2 basalts with E-MORB signatures have high Ba/TiO_2 ratios (>70), indicating a contribution of the enriched mantle source to magma generation (Fig. 9). These basalts are medium-K mildly alkaline basalts and younger than 3.1 Ma. The PR3 basalts (N-MORB) older than 3.5 Ma, however, are very low in Ba/TiO_2 ratios (< 20) and likely to be a product from depleted mantle source. It is remarkable that there are no transitional basalts indicating a mixing relationship between the N- and E-type basalts. The sources could not change rapidly from a depleted to an enriched mantle in the absence of influx of new materials during a short time interval less than ca. 0.5 m.yr. It is thus likely that the source mantle beneath the APR was intrinsically heterogeneous when the magma was formed. In addition, the E-MORB could be produced from the contribution of enriched materials such as metasomatized veins or pyroxenite veins/blobs to mantle melting.

The HREE depletion is typical for the signature of residual garnet (le Roux et al., 2002; Nauret et al., 2003; Ionov, 2004). From the LREE enrichment and the HREE depletion of E-MORB, the most plausible source material could be the garnet pyroxenite (including recycled oceanic crust) (Hirschmann and Stolper, 1996; Nauret et al., 2003) or the subduction-modified mantle (Donelly et al., 2004). However, garnet is unstable at the MOR setting except for high pressure conditions (28-30 kbar) (Robinson and Wood, 1998). Nevertheless, garnet can persist on the solidus of pyroxenite to much lower pressures than that of peridotite, and the upper mantle may contain 2-5% pyroxenite (Hirschmann and Stolper, 1996). Typical mantle pyroxenites have lower solidus temperature than peridotites (e.g., by 150-200 °C at 20-30 kbar) and are capable of producing large melt fractions at depths where peridotite is either solid or only slightly melted (Hirschmann and Stolper, 1996). If pyroxenite is present in the MOR setting, it may produce a garnet-like signature of E-MORB. Also conductive cooling by slow-spreading may deepen the final depth of mantle melting, resulting in the decreased melting degree. Therefore, pyroxenite would preferentially participate in the melting at low-extent melting regime when the E-MORB of the APR were formed.

Because there is no peridotite complementary to MORB from APR, it is difficult to exactly model the mantle process beneath APR. In addition, the available E-MORB data cannot place exact constraints on the enriched material at the APR. Thus, we assumed that the enriched material has considerable amount of garnet.

The Ba/La versus Sm/La ratios are illustrated together

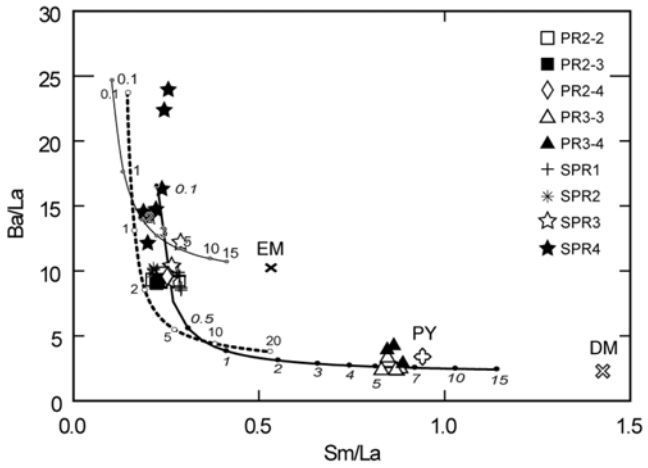

Fig. 10. Ba/La vs. Sm/La ratios of the APR basalts. Modal melting equation, $C_l=C_o/[D_o+F(1-D_o)]$ is performed. Dashed, thin, and thick curves represent the partial melting of pyroxenite (PY), enriched mantle (EM), and depleted mantle (DM), respectively, calculated assuming a batch melting. Partition coefficients and source compositions of EM, DM, and PY are adopted from Donnelly et al. (2004), Salters and Stracke (2004), and Sun and McDonough (1989).

with modal melting models from various sources to evaluate possible source materials and extent of melting (Fig. 10). Large degree of melting (up to 7%) from a depleted mantle source is required for the formation of the older N-type PR3 magma. This is fairly possible, when compared to other N-MORB from ocean ridges worldwide, though the calculated melting degree is slightly lower. The slight enrichment in incompatible elements of the PR3 basalts relative to N-MORB average (Fig. 7a) may indicate smaller degree of partial melting. However, extremely low-degree partial melting (less than 0.3%) is necessary to produce the younger, E-type SPR and PR2 magmas, if the source is composed of a depleted mantle alone, but this extent of melting seems to be too low to produce proper quantity of melts. Instead, if we presume the source as an enriched mantle alone, the E-MORB in the APR could not be produced, because the majority of the E-MORB data are plotted below the calculated melting curve. Therefore, the models given in Figure 10 suggest that probable enriched materials consisting of pyroxenites (recycled oceanic crust) have played an important role for the generation of E-MORB magmas beneath the APR, as well as the melting of the surrounding depleted mantle. If this is the case, the upper mantle beneath the APR may be composed of aggregates of pyroxenites that have been left by the melting of subducted oceanic crust, and peridotites that have been contaminated by the melts from pyroxenites (Blichert-Toft et al., 1999).

As an alternative source material of E-MORB, the metasomatized mantle from the subduction zone cannot be ruled out. Donnelly et al. (2004) suggested that oceanic lithospheric mantle can be enriched by the addition of low-degree melts of subducted crust. However, E-MORB from the metasomatized lithospheric mantle have major element compositions similar to N-MORB. The E-MORB and N-MORB of the APR have different major and trace element chemistries. Therefore, this model alone cannot explain the different geochemistry of two types of the APR basalts.

Taking into account the geochemical characteristics of the N- and E-MORB, we have to assume that the APR upper mantle is a mixture of two compositionally distinct sources: one is a volumetrically small and low-temperature melting component enriched in alkalis and other incompatible elements, and the other is the depleted peridotite host (DMM). In a setting of normal spreading of the APR at > 3.5 Ma, peridotite with higher melting temperature would have melted extensively at shallow level and the signal from enriched materials could have been diluted. On the contrary, in a setting of thickened lithosphere and conductive cooling after the extinction of spreading (< 3.3 Ma), the amount of peridotite-derived, N-MORB melt would become relatively smaller, and the enriched materials with lower melting temperature have more preferentially participated in the melting to produce the E-MORB of the APR.

ACKNOWLEDGMENTS: We thank the captain and crew of R/V *Yuzhmorgeologiya* for their support during 2000-2001 and 2002-2003 summer cruises. This study was supported by KOPRI projects (PE07020; Formation, Evolution and Neotectonics of Antarctica). We also thank Dr. S. -R. Lee and Prof. K.H. Park for their critical reviews and helpful comments.

REFERENCES

Barker, P.F., 1982, The Cenozoic subduction history of the Pacific margin of the Antarctic Peninsula: ridge crest-trench interactions. Journal of Geological Society of London, 139, 787–801.

Blichert-Toft, J., Albarède, F. and Kornprobst, J., 1999, Lu-Hf isotope systematics of garnet pyroxenites from Beni Bousra, Morocco: Implications for basalt origin. Science, 283, 1303–1306.

Choe, W.H., Lee, J.I., Lee, M.J., Hur, S.D. and Jin, Y.K., 2005, New approach on the extinction of spreading at the Phoenix Ridge, Antarctica. Journal of the Petrological Society of Korea, 14, 73–81. (in Korean with English Abstract).

Cooper, K.M., Eiler, J.M., Asimow, P.D. and Langmuir, C.H., 2004, Oxygen isotope evidence for the origin of enriched mantle beneath the mid-Atlantic ridge. Earth and Planetary Science Letters, 220, 297–316.

Donnelly, K.E., Langmuir, C.H. and Goldstein, S.L., 2000, Constraints on the generation of enriched mid-ocean ridge basalts. EOS, 81, 1281.

Donnelly, K.E., Goldstein, S.L., Langmuir, C.H. and Spieglman, M., 2004, Origin of enriched ocean ridge basalts and implications for mantle dynamics. Earth and Planetary Science Letters, 226, 347–366.

Douglass, J., Schilling, J.-G. and Fontignie, D., 1999, Plume-ridge interactions of the Discovery and Shona mantle plumes with the southern mid-Atlantic Ridge (40°-55°S). Journal of Geophysical Research, 104, 2941–2962.

Hanson, G.N. and Langmuir, C.H., 1978, Modelling of major elements in mantle-melt systems using trace element approaches. Geochimica et Cosmochimica Acta, 42, 725–741.

Hirschmann, M.M. and Stolper, E.M., 1996, A possible role for garnet pyroxenite in the origin of the "garnet signature" in MORB. Contributions to Mineralogy and Petrology, 124, 185–208.

Holness, M.B. and Richter, F.M., 1989, Possible effects of spreading rate on MORB isotopic and rare earth composition arising from melting of a heterogeneous source. Journal of Geology, 97, 247–260.

Hur, S.D., Lee, J.I., Lee, M.J. and Kim, Y.D., 2003, Determination of rare earth elements abundance in alkaline rocks by inductively coupled plasma mass spectrometry (ICP-MS). Ocean and Polar Research, 25, 53–62. (in Korean with English Abstract).

Ionov, D., 2004, Chemical variations in peridotite xenoliths from Vitim, Siberia: Inferences for REE and Hf behaviour in the garnet-facies upper mantle. Journal of Petrology, 45, 343–367.

Janney, P.E., Roex, A.P.L. and Carlson, R.W., 2005, Hafnium isotope and trace element constraints on the nature of mantle heterogeneity beneath the Central Southwest Indian Ridge (13°E to 47°E). Journal of Petrology, 46, 2427–2464.

Jaques, A.L. and Green, D.H., 1980, Anhydrous melting of peridotite at 0-15 kbar pressure and the genesis of tholeiitic basalts. Contributions to Mineralogy and Petrology, 73, 287–310.

Kent, A.J.R., Stolper, E.M., Francis, D., Woodhead, J., Frei, R. and Eiler, J., 2004, Mantle heterogeneity during the formation of the North Atlantic Igneous Province: Constraints from trace element and Sr-Nd-Os-O isotope systematics of Baffin Island picrites: Geochemistry Geophysics Geosystems, 5, doi:10.1029/2004GC000743.

Kim, K.J., 2005, Geophysical investigations of the Phoenix Ridge, a fossil spreading center in Drake Passage, Antarctica. Ph.D. thesis, Seoul National University, 156 p.

Klein, E.M. and Langmuir, C.H., 1987, Global correlations of ocean ridge basalt chemistry with axial depth and crustal thickness. Journal of Geophysical Research, 92, 8089–8115.

Krolikowska-Ciaglo, S., Hauff, F., Deyhle, A. and Hoernle, K., 2003, Effects of low temperature seawater alteration. Geophysical Research Abstracts, 5, 01039.

Larter, R.D. and Barker, P.F., 1991, Effects of ridge-trench interaction on Antarctic-Phoenix spreading: Forces on a young subducting plate. Journal of Geophysical Research, 96, 19583–19607.

Lee, J.I., 1994, A study on the development of quantitative analytical program of the granitic rocks using an X-ray Fluorescence. KORDI Report, BSPE 00431-671-7, 43 p. (in Korean with English Abstract).

Lehnert, K., Su, Y. and Langmuir, C.H., 2000, A global geochemical database structure for rocks. Geochemistry, Geophysics, Geosystems, 1, 1999GC000026.

Le Maitre, R.W., Bateman, P., Dudek, A., Keller, J., Lameyre Le Bas, M.J., Sabine, P.A., Schmid, R., Sorensen, H., Streckeisen, A., Woolley, A.R. and Zanettin, B., 1989, A Classification of Igneous Rocks and Glossary of Terms. Blackwell Science, Inc., London, 193 p.

le Roux, P.J., le Roex, A.P. and Schilling, J.-G., 2002, MORB melting processes beneath the southern Mid-Atlantic Ridge (40-55°S): a role for mantle plume-derived pyroxenite: Contributions to Mineralogy and Petrology, 144, 206–229.

Livermore, R., Balanya, J.C., Maldonado, A., Martinez, J.M., Rodriguez-Fernandez, J., Galdeano, C.S., Zaldivar, J.G., Jabaloy, A., Barnolas, A., Somoza, L., Hernandez-Molina, J., Surinach, E. and Viseras, C., 2000, Autopsy on a dead spreading center: The Phoenix Ridge, Drake Passage, Antarctica. Geology, 28, 607–610.

Maldonado, A., Larter, R.D. and Aldaya, F., 1994, Fore-arc tectonic evolutions of the South Shetland margin, Antarctic Peninsula. Tectonics, 13, 1345–1370.

Michael, P.J., Langmuir, C.H., Dick, H.J.B., Snow, J.E., Goldstein, S.L., Graham, D.W., Lehnert, K., Kurras, G., Jokat, W., Mühe, R. and Edmonds, H.N., 2003, Magmatic and amagmatic seafloor generation at the ultraslow-spreading Gakkel ridge, Arctic Ocean. Nature, 423, 956–962.

Mitchell, N.C. and Livermore, R.A., 1998, Spiess Ridge: An axial high on the slow spreading Southwest Indian Ridge. Journal of Geophysical Research, 103, 15457–15471.

Morris, J.D. and Hart, S.R., 1983, Isotopic and incompatible element constraints on the genesis of island arc volcanics from Cold Bay and Amak Island, Aleutians, and implications for mantle structure. Geochimica et Cosmochimica Acta, 47, 2015–2030.

Nauret, F., Abouchami, W., Galer, S.J.G., Hofmann, A.W., Hémond, C., Chauvel, C. and Dyment, J., 2006, Correlated trace element-Pb isotope enrichments in Indian MORB along 18–20°S, Central Indian Ridge. Earth and Planetary Science Letters, 245, 137–152.

Niu, Y. and Batiza, R., 1991, An empirical method for calculating melt compositions produced beneath mid-ocean ridges: Application for axis and off-axis (seamounts) melting. Journal of Geophysical Research, 96, 21753–21777.

Niu, Y. and Hékinian, R., 1997, Spreading rate dependence of the extent of mantle melting beneath ocean ridges. Nature, 385, 326–329.

Niu, Y., Collerson, K.D. and Batiza, R., 1999, Origin of enriched-type mid-ocean ridge basalt at ridges far from mantle plumes: the East Pacific Rise at 11°20 N. Journal of Geophysical Research, 104, 7067–7087.

Perfit, M.R. and Chadwick, Jr., W.W., 1998, Magmatism at mid-ocean ridges: constraints from volcanological and geochemical investigations. In: Buck, W.R., Delaney, P.T., Karson, J.A. and Lagabrielle, Y. (eds.), Faulting and Magmatism at Mid-Ocean Ridges. American Geophysical Union, Washington, D.C., p. 59–115.

Pertermann, M. and Hirschmann, M.M. 2003, Partial melting experiments on a MORB-like pyroxenite between 2 and 3 GPa: Constraints on the presence of pyroxenite in basalt source regions from solidus location and melting rate. Journal of Geophysical Research, 108, doi:10.1029/2000JB000118.

Rhodes, J.M., Morgan, C., and Liias, R.A., 1990, Geochemistry of axial seamount lavas: Magmatic relationship between the Cobb hotspot and the Juan de Fuca ridge, Journal of Geophysical Research., 95, 12713–12733.

Robinson, J. A. C. and Wood, B. J., 1998, The depth of the spinel to garnet transition at the peridotite solidus. Earth and Planetary Science Letters, 164, 277–284.

Salters, V.J.M. and Stracke, A., 2004, Composition of the depleted mantle. Geochemistry, Geophysics, Geosystems. 5, doi:10.1029/2003GC000597.

Shen, Y. and Forsyth, D.W., 1995, Geochemical constraints on initial and final depths of melting beneath mid-ocean ridges. Journal of Geophysical Research, 100, 2211–2237.

Smith, W.H.F. and Sandwell, D.T., 1994, Bathymetric prediction from dense satellite altimetry and sparse shipboard bathymetry, Journal of Geophysical Research, 99, 21803–21824.

Sun, S.-S. and McDonough, W.F., 1989, Chemical and isotopic systematics of oceanic basalts: implications for mantle composition and processes. In: Saunders, A.D. and Norry, M.J. (eds.), Magmatism in the Ocean Basins. Geological Society Special Publication 42, Blackwell Scientific Publications, London, p. 313–345.

Thatcher, W. and Hill, D.P., 1995, A simple model for the fault-generated morphology of slow-spreading mid-ocean ridges. Journal of Geophysical Research, 100, 561–570.

Wei, W., Kastner, M., Rosenbauer, R., Weinstein, Y. and Chan, L., 2004, Cycling of Li, K, Rb, and Cs at Subduction Zones and Ridge Crests With Implications for Ocean Chemistry: Hydrothermal Experiments at 35-350°C and 600 bars. Eos Transactions American Geophysical Union, 85(47), Fall Meeting, Supplement, Abstract V13A–1450.

Whitehead, J.A., Dick, H.J.B. and Schouten, H., 1984, A mechanism for magmatic accretion under spreading centres. Nature, 312, 146–148.

Zindler, A. and Hart, S.R., 1986, Chemical geodynamics. Annual Review of Earth Planetary Sciences, 14, 493–571.

Manuscript received August 1, 2006
Manuscript accepted August 31, 2007